Acta Metall. Sin. (Engl. Lett.), 2016, **29**(4), 326–334
DOI 10.1007/s40195-016-0399-9

Comparative Study on Characteristics and Cytotoxicity of Bifunctional Magnetic-Silver Nanostructures: Synthesized Using Three Different Reducing Agents

Narjes Ebrahimi[1] · Sara Rasoul-Amini[2,3] · Alireza Ebrahiminezhad[4] · Younes Ghasemi[1,3] · Ahmad Gholami[1] · Hassan Seradj[5]

Received: 18 June 2015 / Revised: 17 November 2015 / Published online: 16 March 2016

Abstract Magnetic-silver nanostructures were synthesized via optimized chemical conditions, and their characteristics and cytotoxicity were compared as candidates for the magnetic delivery of silver nanoparticles toward cancer cells. Magnetic-silver nanostructures were prepared through the reduction of silver ions in the presence of iron oxide nanoparticles using three different reducing agents (glucose, maltose and sodium citrate). Their physicochemical characteristics were determined using ultraviolet–visible spectroscopy, X-ray diffraction analysis, transmission electron microscopy, selected area electron diffraction analysis, Fourier transformed infrared spectroscopy, atomic absorption spectroscopy, vibrating sample magnetometry and differential scanning calorimetry. Cytotoxic activities were evaluated against a human liver hepatocellular carcinoma cell line. Fabricated nanostructures, which exhibit differences in size, silver content, magnetic saturation value and cytotoxicity, represent sufficient superparamagnetic properties and considerable cytotoxicity to be suggested as effective tools in magnetic targeting of silver nanoparticles as an approach to cancer therapy.

KEY WORDS: **Bifunctional nanostructure; Magnetic-silver nanostructure; Silver nanoparticle; Cytotoxicity; Reducing agent**

1 Introduction

Multifunctional nanostructures have already attracted great attention in biomedical applications [1]. The combination of two functional structures in a single nanoparticle will obviously result in the combined properties of components [2].

Superparamagnetic iron oxide nanoparticles (SPIONs), such as magnetite (Fe_3O_4), represent attractive features to design hybrid nanostructures for magnetically controllable drug delivery [3] and diagnostic approaches [4], as they can be guided by an external magnetic field toward target areas while they are concurrently functionalized with a bioactive agent [5].

As a promising bioactive candidate to functionalize SPIONs, silver nanoparticles (AgNs) are considered, exhibiting distinctive physiochemical and biological

Available online at http://link.springer.com/journal/40195

✉ Sara Rasoul-Amini
rasoulamini@sums.ac.ir

[1] Department of Pharmaceutical Biotechnology, School of Pharmacy, Shiraz University of Medical Sciences, Shiraz, Fars, Iran

[2] Department of Medicinal Chemistry, School of Pharmacy, Shiraz University of Medical Sciences, Shiraz, Fars, Iran

[3] Pharmaceutical Sciences Research Center, Shiraz University of Medical Sciences, Shiraz, Fars, Iran

[4] Department of Medical Biotechnology, School of Medicine, Fasa University of Medical Sciences, Fasa, Fars, Iran

[5] Department of Pharmacognosy, School of Pharmacy, Shiraz University of Medical Sciences, Shiraz, Fars, Iran

properties: optical and catalytic properties [6], antibacterial [7] and antifungal activities, and cytotoxic activity [8].

Bifunctional magnetic-silver nanostructures (Fe_3O_4–AgNs) are believed to show combined properties of their two components. Although a couple of individual methods [9, 10] has already been reported in regard to the fabrication of Fe_3O_4–AgNs for diagnostic (as surface enhanced Raman spectroscopy (SERS) active agents) [11–14] and catalytic applications [15], the studies on saving the efficacy of each individual component are still considered in the aforementioned bifunctional nanostructures [14].

There are some structural factors (such as particle size [16]) and the incorporated silver into Fe_3O_4–AgNs [17] which obviously affect the pharmacokinetic [18], silver release amount, the interaction with biologic molecules [19] and consequently the resulting biologic activities. Meanwhile, Kvitek et al. and Pal et al. [20, 21] reported the effects of surface chemistry and shapes of silver nanoparticles on antibacterial activity, respectively. In fact, the observed biological properties of the prepared nanoparticles are strongly dependent on the synthesis methods [22]. Thus, the optimization of the synthesis method approaching the final application of target Fe_3O_4–AgNs plays an important role to get desired properties.

Moreover, studies considering cytotoxic effects of Fe_3O_4–AgNs for the magnetic delivery of silver nanoparticles, as cytotoxic agent, toward cancer cells have already been limited [23] as long as antibacterial activity has been mostly focused. Dallas et al. [24] have reported antibacterial activity of phosphotriazine-based magnetically controllable silver nanocomposite. Antibacterial activity of a magnetic nanocomposite of silver and iron oxide nanoparticles was reported by Prucek et al. [17]. Wang et al. [25] reported the antibacterial activity of silver-coated magnetic nanoparticles and Zhang et al. [26] also investigated the antibacterial activity of magnetic-silica Janus nanorod decorated with silver nanoparticles. In the study reported by Di Corato et al. [23] magnetic nanobeads decorated with silver nanoparticles were designed as a cytotoxic agent.

In the present study, the prepared Fe_3O_4 nanoparticles were treated with silver nitrate ($AgNO_3$) to synthesize bifunctional Fe_3O_4–AgN_C, Fe_3O_4–AgN_G and Fe_3O_4–AgN_M, employing three different reducing agents including citrate, glucose and maltose, respectively. Some factors in the synthetic procedure (such as concentration of the applied reducing agents and $AgNO_3$, the order in which reagents are added, and the ideal time of reaction) were evaluated to determine the optimal reaction condition for the preparation of target Fe_3O_4–AgNs.

Physicochemical characteristics and cytotoxicity were compared for three individually synthesized Fe_3O_4–AgNs (Fe_3O_4–$AgN_{(C,\ G\ and\ M)}$) as candidate cytotoxic nanostructures controllable by magnetic field as means to target cancer cells.

2 Experimental

2.1 Chemicals

Ferrous sulfate heptahydrate ($FeSO_4{\cdot}7H_2O$, >99.5%), ferric chloride hexahydrate ($FeCl_3{\cdot}6H_2O$, >99%), silver nitrate ($AgNO_3$), maltose monohydrate (>95%), glucose monohydrate (99%) and ammonia solution (25% w/w) were all purchased from the Merck Company (Germany). Sodium citrate dihydrate was purchased from Kimia Mavad (Iran), and 3-(4,5-dimethylthiazol-2-yl)-2,5-diphenyltetrazolium bromide (MTT) and phosphate-buffered saline (PBS) (10×, pH 7.4) were obtained from the Sigma-Aldrich Company. Fetal bovine serum (FBS) was obtained from Gibco Invitrogen, and RPMI 1640 was obtained from Shell Max.

All chemicals were of analytical grade, and all aqueous solutions were prepared using deionized water obtained through the Millipore Direct-Q3 UV system.

2.2 Synthesis of Fe_3O_4 Nanoparticles

Fe_3O_4 nanoparticles were synthesized by the chemical co-precipitation method [27, 28]. First, $FeSO_4$ (0.6 g) and $FeCl_3$ (1.75 g) were dissolved in 50 mL of deionized water (molar ratio of 1:1.75), and the obtained solution was stirred continuously for 1 h under nitrogen at 70 °C. Then, ammonium hydroxide 32% w/w (5 mL) was rapidly injected, and the suspension was vigorously stirred for another hour after which it was allowed to cool to room temperature. The magnetic nanoparticles thus obtained were subjected to magnetic separation, washed with deionized water for several times and dried in an oven at 50 °C overnight.

2.3 Synthesis of Bifunctional Fe_3O_4–AgNs Using Glucose or Maltose (Fe_3O_4–$AgN_{(G\ and\ M)}$)

AgNs were initially prepared by reducing silver in the complex of $[Ag\ (NH_3)_2]^+$ using maltose or glucose according to the modified Tollens process [29, 30] in the presence of the previously prepared Fe_3O_4 nanoparticles [17, 31]. For this purpose, three individual aqueous solutions were prepared as follows: silver solution (solution A): 35 mL containing 10 mmol/L $AgNO_3$ and 20 mmol/L NH_4OH; reducing solution (solution B): 10 mL containing 200 mmol/L glucose or maltose; and activating solution (solution C): 3 mL containing 80 mmol/L NaOH and 80 mmol/L NH_4OH.

Initially, 12 mL of solution A was pipetted into 17 mL of Fe_3O_4 aqueous suspension (obtained by dispersing 50 mg Fe_3O_4 in deionized water using probe sonication). Then, 5 mL of solution B was added drop by drop to the initial solution in the sonication bath, and the pH value was adjusted to 9 using solution C. After 30 min, 10 mL of solution A was added to the obtained mixture in two divided portions, followed by the addition of solution B (2.5 mL). Adjusting pH value to 9, sonication was continued for an additional period of 30 min. This step was repeated, whereupon the obtained nanoparticles Fe_3O_4–$AgN_{(G\ and\ M)}$ were separated from silver ions (Ag^+) and free AgNs by a permanent magnet, rinsed for several times with deionized water and dried overnight in an oven at 50 °C. The Fe_3O_4–AgNs thus obtained were called Fe_3O_4–AgN_G when glucose was applied as the reducing agent and called Fe_3O_4–Ag_M in the case of maltose as the reducing agent.

2.4 Synthesis of Bifunctional Fe_3O_4–AgNs Using Sodium Citrate (Fe_3O_4–AgN_C)

The target Fe_3O_4–AgNs were synthesized by modifying the procedure reported by Lee and Meisel for silver nanoparticle preparation [32]. First, 10 mL of $AgNO_3$ solution (10 mmol/L) was added to 17 mL of Fe_3O_4 suspension (obtained by dispersing 50 mg Fe_3O_4 in deionized water using probe sonication). Then, 5 mL of sodium citrate solution (400 mmol/L) was added drop by drop to the prepared suspension. Stirring under reflux condition for 1 h, 10 mL of $AgNO_3$ (10 mmol/L) was added in two individual portions followed by the addition of 3 mL of sodium citrate solution (400 mmol/L). The prepared Fe_3O_4–AgN_C was subjected to magnetic separation, washed to eliminate free AgNs and finally dried overnight in an oven at 50 °C.

2.5 Nanoparticle Characterization

UV–Vis analyses were performed with a PG Instruments T80 + UV/Vis spectrophotometer over the wavelength range of 300–700 nm. The crystallinity of the powders was studied by X-ray diffraction (XRD) using a Siemens D5000 diffractometer with Ni-filtered Cu$K\alpha$ radiation ($\lambda = 0.15406$ nm). The particle size distribution and morphology of the prepared Fe_3O_4–AgNs were characterized by transmission electron microscopy (TEM), and selected area electron diffraction (SAED) patterns were obtained with a Philips CM30, operated at HT 150 kV. The particle size of Fe_3O_4–AgN_G was analyzed using a Microtrac Nanotrac wave particle size analyzer (Microtrac, USA). To analyze the infrared spectra of the samples, a Bruker Vertex 70 Fourier transformed infrared (FTIR) spectrometer was employed, applying KBr pellets. The silver content of the Fe_3O_4–AgNs was measured using atomic absorption spectroscopy (AAS) on a SavantAA device (CBG Science Equipment, Australia), applying $AgNO_3$ as the standard solution. The magnetic properties were measured on a vibrating sample magnetometer (VSM) at room temperature (Meghnatis Daghigh Kavir Co.). Differential scanning calorimetry (DSC) analyses were conducted using a BAHR Thermoanalyse DSC 302 over a temperature range of 25–499 °C, using Al_2O_3 as the standard.

2.6 Cell Culture

The HepG2 carcinoma cell line was provided by the Iranian Branch of the Pasteur Institute, National Cell Bank of Iran (NCBI: C-158). They were cultured in RPMI media with 10% FBS in a 5% CO_2 incubator at 37 °C.

2.7 Cytotoxicity Evaluation of Bifunctional Fe_3O_4–AgNs

Stock solutions (1 mg/mL) of the synthesized Fe_3O_4–AgNs in sterile phosphate-buffered solution (PBS) were diluted with cell culture medium to provide test concentrations. HepG2 cells, seeded in 96-well plates (10^4 cells/well) at 37 °C and 5% CO_2, were exposed to the appropriate concentrations (1, 10, 25, 50, 75, 100 μg/mL) of nanoparticle solutions (Fe_3O_4–AgNs) and naked Fe_3O_4 for 48 h (number of experiments: 3). The cells were then treated with dimethylthiazolyl diphenyltetrazolium bromide (MTT) solution for 3 h to evaluate the effect of nanoparticles on cell viability [33]. Finally, the absorbance was measured on a microplate reader (Bio-Tek, Power Wave XS2) at the wavelength of 540 nm as a reference of mitochondrial reduction of MTT (3-(4, 5-dimethylthiazol-2-yl)-2, 5-diphenyltetrazolium bromide) to formazan. The viability of the test samples was expressed as a percentage of the control group.

2.8 Statistical Analysis

Statistical analysis was performed by applying the one-way analysis of variance (ANOVA), in which p value <0.05 was regarded as significant. The data were presented as the mean ± SD obtained from the experiments, which were conducted in triplicate.

3 Results and Discussion

3.1 Characterization of Prepared Bifunctional Fe_3O_4–AgNs

3.1.1 UV–Vis Absorption Measurements

As we monitored the synthesis process, the UV–Vis spectral features of the initial Fe_3O_4 gradually changed with the appearance of an absorption peak in the wave length range of 400–440 nm, due to surface plasmon resonance of silver confirming the incorporation of silver in the target Fe_3O_4–AgNs. Similar UV–Vis spectrums were observed in the study by Eskandari and Ghourchian [34].

By comparing the UV spectra for the synthesized Fe_3O_4–AgNs (Fig. 1: C, G, M and F), broad absorption peak and slight red shift to approximately 430 nm indicate a wider size distribution and larger particle size for Fe_3O_4–AgN_C (Fig. 1: C).

3.1.2 XRD, SAED, TEM and DLS Analyses

Figure 2 (C, G, M and F) illustrates XRD patterns for the pure Fe_3O_4 and the synthesized bifunctional Fe_3O_4–$AgN_{(C,\ G\ and\ M)}$. Characteristic peaks were observed at 2θ values of 30.1°, 35.5°, 43.1°, 53.5°, 57.0° and 62.6°, which are approved for pure Fe_3O_4 and correspond to the (220), (311), (400), (422), (511) and (440) planes of crystalline

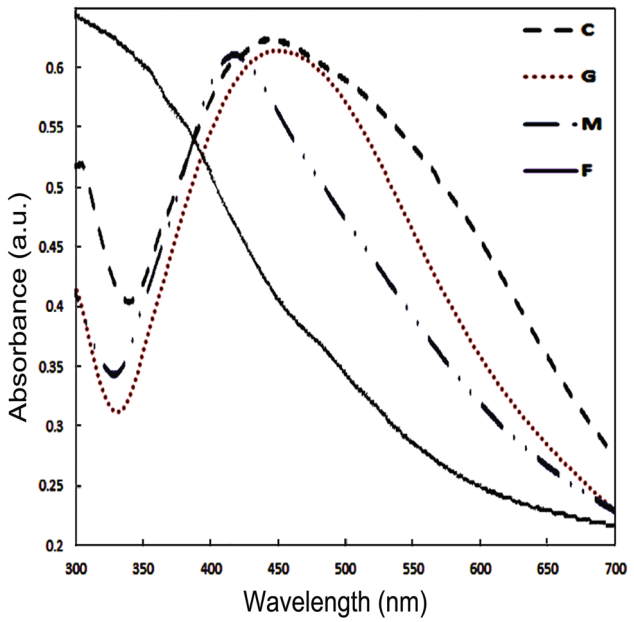

Fig. 1 UV–Vis absorption spectra of Fe_3O_4–AgN_C (C), Fe_3O_4–AgN_G (G), Fe_3O_4–AgN_M (M) and Fe_3O_4 (F). The appearance of an absorption peak in the wave length range of 400–440 nm, due to the surface plasmon resonance of silver, is observed for C, G and M compared with F

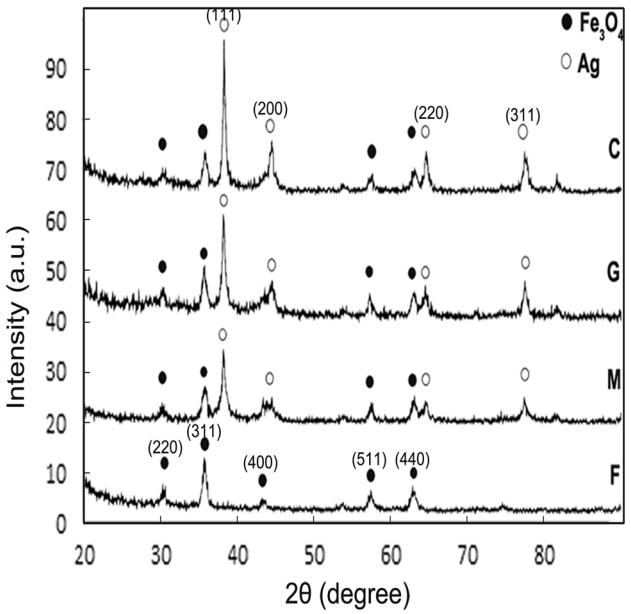

Fig. 2 XRD patterns of Fe_3O_4–AgN_C (C), Fe_3O_4–AgN_G (G), Fe_3O_4–AgN_M (M) and Fe_3O_4 (F). The diffraction peaks of both silver and Fe_3O_4 are observed in C, G and M compared with F (measured with $\lambda = 0.15406$ nm)

Fe_3O_4. XRD patterns for Fe_3O_4–$AgN_{(G,\ M,\ C)}$ illustrate the diffraction peaks of silver ($2\theta = 38.1°$, 44.4°, 64.4°, 77.5° and 81.5°, which correspond to the (111), (200), (220), (311) and (222) planes of cubic Ag) as well as Fe_3O_4, these being consistent with ICDD PDF2 references (JCPDF No. 01-075-0033 of Fe_3O_4; JCPDF No. 00-001-1167 and 00-004-0783 of Ag in Fe_3O_4–$AgN_{(G\ and\ C)}$ and Fe_3O_4–AgN_M, respectively) and confirm the coexistence of Fe_3O_4 and AgN in the bifunctional Fe_3O_4–AgNs thus obtained [14, 35].

SAED patterns of Fe_3O_4–AgNs are presented as insets of Fig. 3 (the patterns of Fe_3O_4–AgN_G and Fe_3O_4 (G-F) are compared, and the corresponding planes are also defined).

The spotted concentric rings reveal the crystalline structure of the synthesized nanostructures. Five diffraction rings are defined in the SAED pattern of Fe_3O_4 which can be assigned to (220), (311), (400), (422) and (511) planes, respectively, of Fe_3O_4. These are in consistent with the XRD results and the standard reference values for Fe_3O_4 (interplanar spacings (d) of 0.29, 0.25, 0.209, 0.17 and 0.16 nm for (220), (311), (400), (422) and (511) planes, respectively). The obtained patterns and interplanar spacings (d) of Fe_3O_4 are also in agreement with those reported by Caruntu et al. and Hui et al. [36, 37].

In the patterns of Fe_3O_4–AgNs, seven diffraction rings were observed and the first ring might be assigned to the (220) plane of Fe_3O_4. It might be possible that the patterns of Fe_3O_4 and Ag coincidence in the next four rings (a similar observation was mentioned about Fe oxide/Au

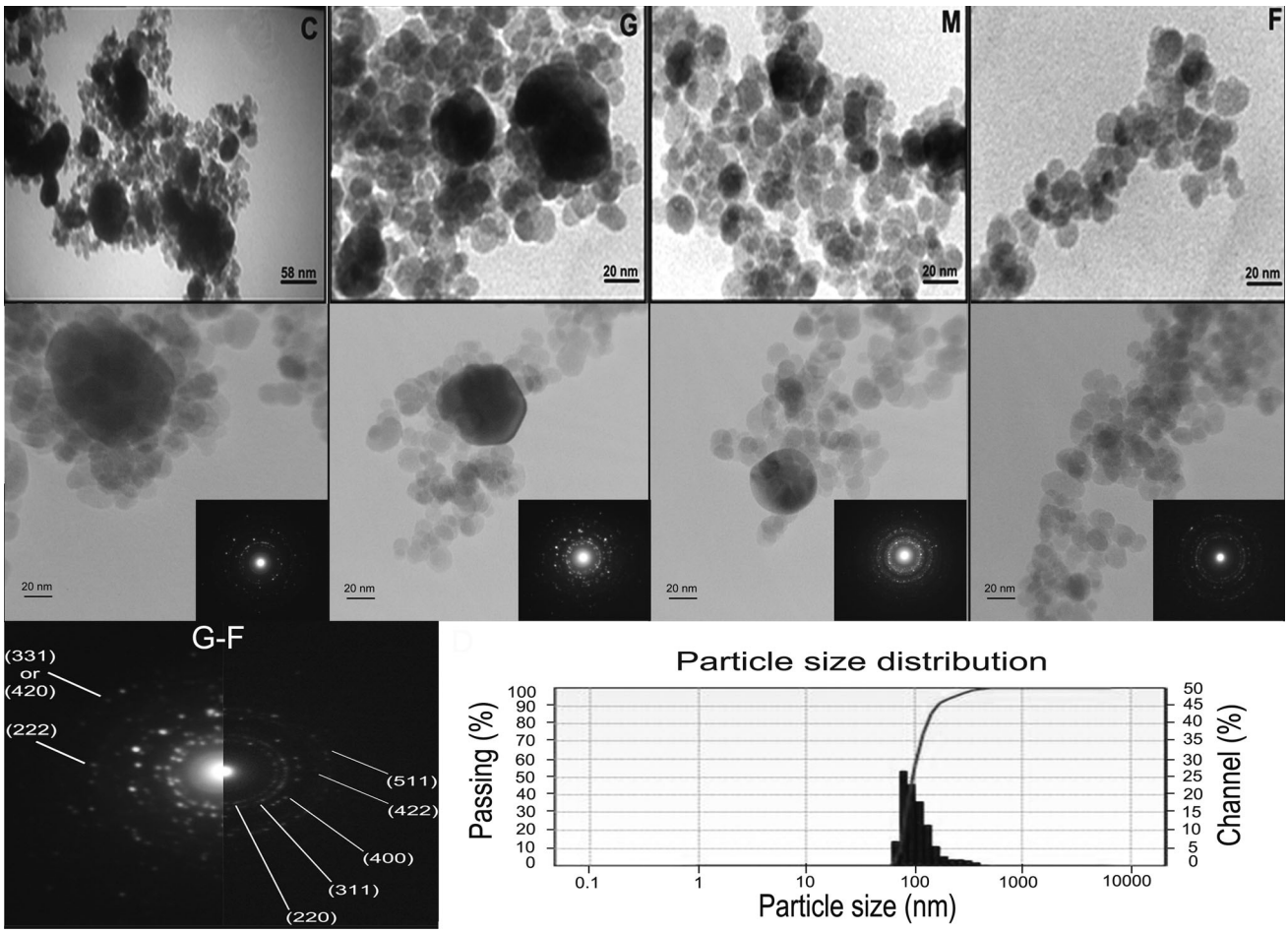

Fig. 3 TEM images and corresponding SAED patterns of Fe_3O_4–AgN_C (C), Fe_3O_4–AgN_G (G), Fe_3O_4–AgN_M (M) and Fe_3O_4 (F); compared SAED patterns of Fe_3O_4–AgN_G and Fe_3O_4 (G–F); DLS analysis of Fe_3O_4–AgN_G (D)

core–shell structure in the study reported by Lu et al. [38]). There are also two more diffraction rings which might be attributed to (222) and (331) or (420) planes, respectively, of the crystalline silver, according to the reference files for patterns and interplanar spacings (*d*) of silver (0.236, 0.204, 0.145, 0.123, 0.118, 0.094 and 0.092 nm for (111), (200), (220), (311), (222), (331) and (420) planes, respectively) and also in agreement with the reported patterns of silver in other studies [39, 40].

TEM images for the pure initial Fe_3O_4 nanoparticles indicate uniform spherical nanoparticles with narrow size distribution showing an average diameter of approximately 11 nm (Fig. 3: F). TEM images obtained in regard to the bifunctional Fe_3O_4–AgNs revealed the coexistence of Fe_3O_4 and AgN [15, 17] in which AgNs seem to be surrounded by Fe_3O_4 nanoparticles (consistent with initial Fe_3O_4 nanoparticle size). This structure is somewhat similar to the reported structure for γ-Fe_2O_3@Ag in the study reported by Prucek et al., in which this kind of structure was synthesized by using γ-Fe_2O_3 nanoparticles with smaller particle size than that of silver nanoparticles (compared to Ag@Fe_3O_4 in which silver nanoparticles had smaller size) [17].

The synthesized nanostructures have higher polydispersity with the average diameters of approximately 54, 32 and 23 nm for incorporated silver nanoparticles into Fe_3O_4–AgN_C, Fe_3O_4–AgN_G and Fe_3O_4–AgN_M, respectively (Fig. 3: C, G and M).

The crystalline size of Fe_3O_4 and Ag nanoparticles was also calculated, using Scherrer's formula, to be 11.77 nm for Fe_3O_4 and 21.32 and 28.66 nm for incorporated silver nanoparticles into Fe_3O_4–AgN_M and Fe_3O_4–$AgN_{(G\ and\ C)}$, respectively. In the present study, more intensity was observed in the peaks which are assigned to silver, along with increase in silver content in Fe_3O_4–$AgN_{(G\ and\ C)}$. As discussed in the study reported by Trang et al. [41], the observed increase in the intensity of silver peaks in XRD patterns was due to the increase in silver crystalline size as a result of increase in the silver sell thickness. In the case of Fe_3O_4, Fe_3O_4–AgN_M and Fe_3O_4–AgN_G, the crystalline

sizes are in consistency with the silver nanoparticle sizes calculated based on TEM images, but the difference in the calculated size for Fe_3O_4–AgN_C might be due to the aggregation of nanoparticles.

In order to have more information about the overall sizes of Fe_3O_4–AgNs, the particle size of Fe_3O_4–AgN_G was also analyzed using DLS, which was measured as 97.1 nm (Fig. 3: D). This particle size is the size of silver nanoparticles, which are surrounded by Fe_3O_4 nanoparticles.

3.1.3 FTIR Analysis

Representative FTIR spectra for the pure Fe_3O_4 nanoparticles and the synthesized Fe_3O_4–AgNs (Fig. 4: C, G, M and F) reveal the absorption band at approximately 440 and 600 cm^{-1}, showing the characteristic peaks for Fe–O stretching. The observed peaks at about 1630 (CO) and 3430 cm^{-1} for Fe_3O_4 corresponded to the deforming and stretching vibrations of the hydroxyl (OH) group [42].

Slight band shifts appeared for the Fe_3O_4–AgNs at the aforementioned wavelengths, due to the probable interactions caused by the presence of the applied reducing agents [43].

Meanwhile, moderate decrement in the intensity of the peak for the OH group in FTIR curves, which is assigned to the hydroxyl ions or water molecules coordinated with unsaturated atoms of the surface of Fe_3O_4 [28], might be due to the new, probable superficial interactions, which can be caused by coexistence of Fe_3O_4 and AgN in the target bifunctional Fe_3O_4–AgNs.

3.1.4 Atomic Absorption Spectroscopy (AAS)

Employing AAS, the highest silver content was calculated for Fe_3O_4–AgN_G to be 33.33% (w/w). The silver content was found to be 31.5% and 26.36% (w/w) for Fe_3O_4–AgN_C and Fe_3O_4–AgN_M, respectively.

3.1.5 VSM Analysis

The plots of magnetization versus magnetic field (*M–H*) at room temperature indicate sufficient magnetic response to an external magnetic field as well as the absence of hysteresis in Fe_3O_4 and the synthesized Fe_3O_4–AgNs (Fig. 5: C, G, M and F). Thus, the superparamagnetic properties of the samples are attributed to the small size of the synthesized Fe_3O_4 nanoparticles which have not been perturbed by the incorporation of silver nanoparticles.

Small changes were observed in the saturation magnetization (M_s) values for our individual Fe_3O_4–AgNs (44.07, 38.43 and 38.23 emu/g for Fe_3O_4–AgN_M, Fe_3O_4–AgN_C and Fe_3O_4–AgN_G, respectively) as compared to 60.05 emu/g for Fe_3O_4 nanoparticles [44]. According to the report by Dallas et al., the lower M_s value can be assigned to the content ratio of silver as a nonmagnetic component to Fe_3O_4 in the target bifunctional nanostructures. Therefore, the weight percent for silver can theoretically be calculated as 26.6%, 36% and 36.34% (w/w) for Fe_3O_4–AgN_M, Fe_3O_4–AgN_C and Fe_3O_4–AgN_G, respectively [24], which are somewhat in accordance with the AAS results.

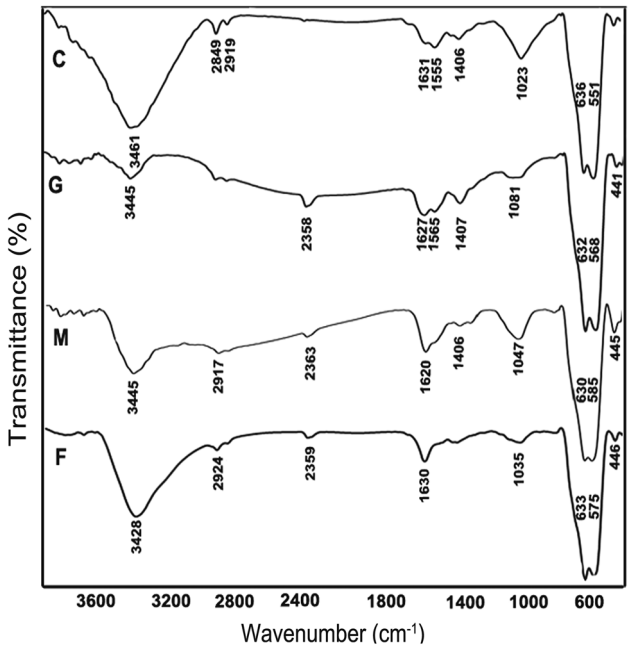

Fig. 4 FTIR spectra of Fe_3O_4–AgN_C (C), Fe_3O_4–AgN_G (G), Fe_3O_4–AgN_M (M) and Fe_3O_4 (F) (applying KBr pellets)

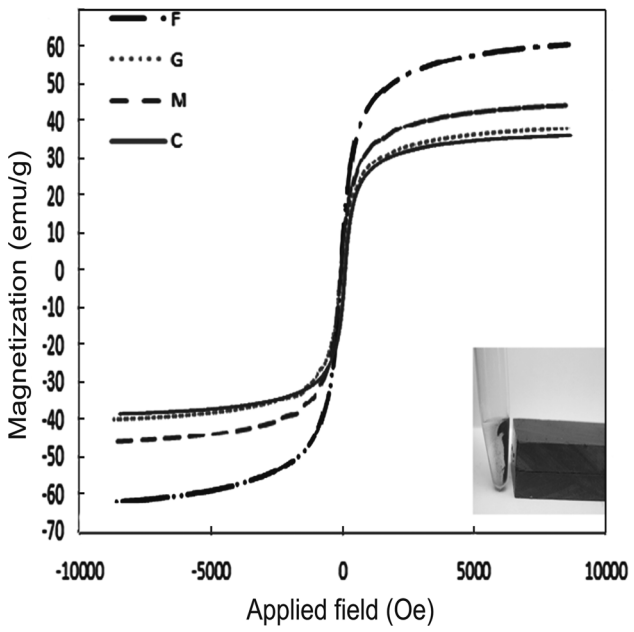

Fig. 5 Saturation magnetization curves of Fe_3O_4–AgN_C (C), Fe_3O_4–AgN_G (G), Fe_3O_4–AgN_M (M) and Fe_3O_4 (F) (measured at room temperature) and magnetic field applied to attract Fe_3O_4–AgNs

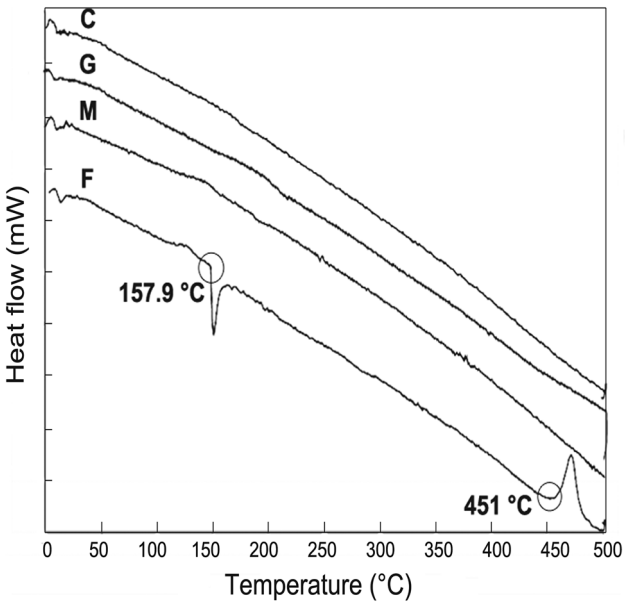

Fig. 6 DSC curves of Fe_3O_4–AgN_C (C), Fe_3O_4–AgN_G (G), Fe_3O_4–AgN_M (M) and Fe_3O_4 (F) (Al_2O_3 as standard)

3.1.6 DSC Analysis

The DSC curves are individually depicted for pure initial Fe_3O_4 and target Fe_3O_4–$AgN_{(C,\ G\ and\ M)}$ in Fig. 6 (C, G, M and F). The endothermic peak centered at 157.9 °C can be assigned to the change in crystallinity, whereas the exothermic peak has been indicated at 451.0 °C corresponding to the transformation of maghemite to hematite for Fe_3O_4 [35]; as mentioned in the literature [45], the temperature in which this transformation occurs is related to the size of maghemite nanoparticles.

The DSC results indicate the prevention of any thermal change which confirms the increased stability in crystal structure of the synthesized Fe_3O_4–AgNs rather than pure Fe_3O_4 nanoparticles in thermal treatment [35].

3.2 Comparative Characteristics of Prepared Fe_3O_4–AgNs

The above-mentioned results (subsections of 3.1) led us to assume that the particle size, incorporated silver content and resulted magnetic saturation value might be variable in the synthesized bifunctional Fe_3O_4–AgN considering the synthesis conditions and reagents such as the applied reducing agent in this study (Table 1).

It was observed that the amount of incorporated silver and particle size in the target Fe_3O_4–AgNs were, respectively, reduced to 26.36% (w/w) and 23 nm when a strong reducing agent (maltose) was applied, supposedly due to its higher reduction rate.

Based on the results, it can be concluded that citrate ions lead to the preparation of larger target Fe_3O_4–AgN_C in wider dispersion as compared to the use of saccharides as the reducing agents for Fe_3O_4–$AgN_{(G\ and\ M)}$.

To compare the applied synthetic methods, the reduction rate, number of formed silver nuclei, size and finally incorporated silver content in the target Fe_3O_4–$AgN_{(G\ and\ M)}$ seem to be managed by $[Ag(NH_3)_2]^+$ as a silver reservoir [17]. As reported by Pillai and Kamat [46] about silver nanoparticle formation using citrate reduction method, it might be assumed that in the preparation of Fe_3O_4–$AgN_{(C)}$, citrate ions, when employed as reducing and stabilizing agents, provide complexes with the initial AgNs and make particles grow subsequently. Meanwhile, low and high pressures in sonication result in uniform and monodisperse nanoparticles at high yield, thereby preventing the aggregation of nanoparticles [15, 47].

3.3 Cytotoxicity Evaluation

The concentration-dependent manner of toxicity for test Fe_3O_4–AgNs was confirmed according to cell viability against HepG2 cell line as a result of MTT assay (Fig. 7). The cell viability values thus obtained reflect significant cytotoxic activities for the test Fe_3O_4–AgNs at concentrations ranging from 1 to 100 μg/mL (as compared to pure Fe_3O_4) within 48 h. The exposure to 50 μg/mL of Fe_3O_4–AgN_G produced a 76% decrease in cell viability, which increased to 86% at the concentration of 100 μg/mL. The concentrations of 50 μg/mL and 100 μg/mL for Fe_3O_4–AgN_C induced 68% and 82% decreases in cell viability, respectively. At concentrations of 1–25 μg/mL, there was no significant difference between Fe_3O_4–AgN_G and Fe_3O_4–AgN_C.

Fe_3O_4–AgN_M exhibited the least cytotoxic activity compared to nanostructures with higher content of silver (Fe_3O_4–AgN_G and Fe_3O_4–AgN_C). At the concentration of 50 μg/mL, Fe_3O_4–AgN_G possessing silver content of 33.33% (w/w) induced 76% cytotoxicity, which is higher than the 68% and 45% obtained for Fe_3O_4–AgN_C and

Table 1 Comparative characteristics (M_s value, particle size and silver content) and cytotoxicity of the synthesized Fe_3O_4–AgNs (calculated EC_{50})

Synthesized nanostructures	M_s (emu/g)	Particle size (nm)	Silver content (%, w/w)	Calculated EC_{50} (μg/mL)
Fe_3O_4–AgN_G	38.23	32	33.33	25
Fe_3O_4–AgN_C	38.43	54	31.5	31.84
Fe_3O_4–AgN_M	44.07	23	26.36	50.89
Fe_3O_4	60.05	11	–	>100

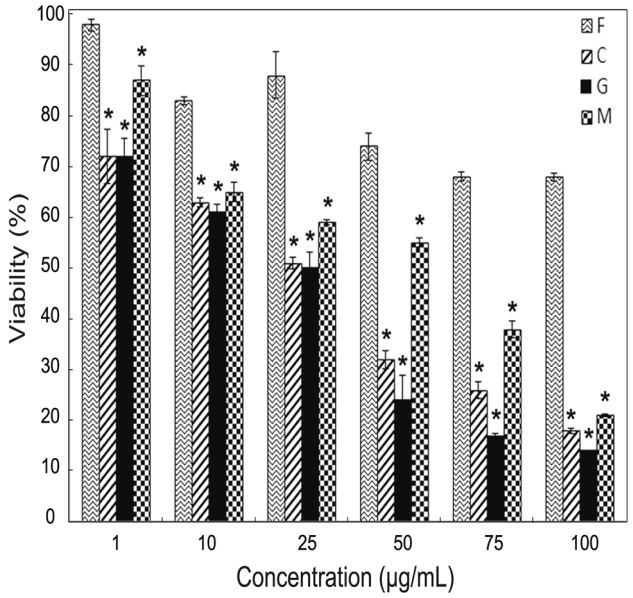

Fig. 7 Cytotoxic activity of Fe_3O_4–AgN_C (C), Fe_3O_4–AgN_G (G), Fe_3O_4–AgN_M (M) and Fe_3O_4 (F). The percent of HepG2 cell viability exposed to the synthesized Fe_3O_4–AgNs at the concentrations of (1, 10, 25, 50, 75, 100 μg/mL) for 48 h, compared with control, according to MTT assay. All data are presented as mean ± SD (standard deviation) (number of experiments = 3). Asterisks (*) represent the statistically significant difference compared with Fe_3O_4

Fe_3O_4–AgN_M having 31.5% and 26.36% (w/w) of silver content, respectively (Table 1). Thus, the higher the silver content of Fe_3O_4–AgN, the greater the cytotoxicity we observed against HepG2 cell line in this study (Table 1).

The effective concentration showing 50% cytotoxicity (EC_{50}) against the HepG2 cell line was predicted as 25 μg/mL for Fe_3O_4–AgN_G and 31.84 μg/mL for Fe_3O_4–AgN_C. However, Fe_3O_4–AgN_M possessing lower silver content exhibited a similar level of cytotoxicity at concentrations above 50 μg/mL (Table 1).

Numerous investigations have reported higher cytotoxicity of silver nanoparticles in regard to their contact surface area, which increased as the particle size was reduced [48]. However, in the case of multifunctional nanostructures the small size of bioactive nanoparticles is not the only effective factor in the level of cytotoxicity. In the case of the synthesized nanostructures in this study (Fe_3O_4–AgNs), it appears to be that the cytotoxic effect (against the HepG2 cell line) is generally governed more by silver content than by particle size. The obtained results are in consistent with the investigations of Prucek et al. [17], in which the higher cytotoxic effects of the γ-Fe_2O_3@Ag nanocomposite were explained by the higher amount of silver compared to Ag@Fe_3O_4 nanocomposite possessing lower amount of silver nanoparticles as long as smaller size.

4 Conclusions

Bifunctional Fe_3O_4–AgNs with various distinct characteristics were individually synthesized using three different reducing agents, in each case by following the optimized synthetic methods. The biomedical potential of the synthesized nanostructures was then evaluated as cytotoxic agents for the magnetic targeting of cancer cells.

The synthesized Fe_3O_4–$AgN_{(G\ and\ C)}$ possessing higher silver content (approximately 33% and 31% (w/w), respectively) and larger particle size (32 and 54 nm, respectively) had relatively higher cytotoxic effects than Fe_3O_4–AgN_M with lower silver content (approximately 26% (w/w)) and smaller particle size (23 nm). The observed results explained the role of silver content in cytotoxic effects of the synthesized Fe_3O_4–AgNs. Although Fe_3O_4–$AgN_{(G\ and\ C)}$ exhibited lower magnetic responses in comparison with Fe_3O_4–AgN_M, the magnetic level is enough to be easily controlled by an external magnetic field, leading us to propose that Fe_3O_4–AgNs can be good candidates for the magnetic targeting of cancer cells. The synthesized Fe_3O_4–AgNs possessing sufficient silver content (responsible factor for cytotoxicity) and considerable magnetic saturation values (supplier factor for magnetic field response) are introduced as attractive candidates in magnetic delivery of silver nanoparticles toward cancer cells.

Acknowledgments This work was financially supported by Shiraz University of Medical Sciences, Shiraz, Iran (Grant Number 92-6587).

References

[1] S. Chidambaram, K. Baskaran, S.J. Samuel, B. Pari, A.R. Sujatha, S. Muthusamy, Mater. Sci. Forum **781**, 1 (2014)
[2] S. Behrens, Nanoscale **3**, 877 (2011)
[3] A.S. Lubbe, C. Alexiou, C. Bergemann, J. Surg. Res. **95**, 200 (2001)
[4] M. Mahmoudi, S. Sant, B. Wang, S. Laurent, T. Sen, Adv. Drug Deliv. Rev. **63**, 24 (2011)
[5] H. Peng, X. Zhang, Y. Wei, W. Liu, S. Li, G. Yu, X. Fu, T. Cao, X. Deng, J. Nanomater. **2012**, 10 (2012)
[6] M.A. Subhan, M. Awal, T. Ahmed, M. Younus, Acta Metall. Sin. (Engl. Lett.) **27**, 223 (2014)
[7] K. Jurczyk, A. Miklaszewski, K. Niespodziana, M. Kubicka, M. Jurczyk, M. Jurczyk, Acta Metall. Sin. (Engl. Lett.) **28**, 467 (2015)
[8] C. You, C. Han, X. Wang, Y. Zheng, Q. Li, X. Hu, H. Sun, Mol. Biol. Rep. **39**, 9193 (2012)
[9] X.M. Liu, Y.S. Li, Mater. Sci. Eng. **29**, 1128 (2009)

[10] E. Iglesias-Silva, J. Rivas, L. León Isidro, M. López-Quintela, J. Non-Cryst. Solids **353**, 829 (2007)
[11] K. Kim, H.J. Jang, K.S. Shin, Analyst **134**, 308 (2009)
[12] B.H. Jun, M.S. Noh, J. Kim, G. Kim, H. Kang, M.S. Kim, Y.T. Seo, J. Baek, J.H. Kim, J. Park, Small **6**, 119 (2010)
[13] J.E. Choi, S. Kim, J.H. Ahn, P. Youn, J.S. Kang, K. Park, J. Yi, D.Y. Ryu, Aquat. Toxicol. **100**, 151 (2010)
[14] J. Chen, Z. Guo, H.B. Wang, M. Gong, X.K. Kong, P. Xia, Q.W. Chen, Biomaterials **34**, 571 (2012)
[15] X. Zhang, W. Jiang, X. Gong, Z. Zhang, J. Alloy. Compd. **508**, 400 (2010)
[16] A. Panacek, L. Kvitek, R. Prucek, M. Kolar, R. Vecerova, N. Pizurova, V.K. Sharma, T. Nevecna, R. Zboril, J. Phys. Chem. B **110**, 16248 (2006)
[17] R. Prucek, J. Tucek, M. Kilianova, A. Panacek, L. Kvitek, J. Filip, M. Kolar, K. Tomankova, R. Zboril, Biomaterials **32**, 4704 (2011)
[18] P. Aggarwal, J.B. Hall, C.B. McLeland, M.A. Dobrovolskaia, S.E. McNeil, Adv. Drug Deliv. Rev. **61**, 428 (2009)
[19] D. Dutta, S.K. Sundaram, J.G. Teeguarden, B.J. Riley, L.S. Fifield, J.M. Jacobs, S.R. Addleman, G.A. Kaysen, B.M. Moudgil, T.J. Weber, Toxicol. Sci. **100**, 303 (2007)
[20] S. Pal, Y.K. Tak, J.M. Song, Appl. Environ. Microb. **73**, 1712 (2007)
[21] L. Kvitek, A. Panáček, J. Soukupova, M. Kolar, R. Vecerova, R. Prucek, M. Holecová, R. Zboril, J. Phys. Chem. C **112**, 5825 (2008)
[22] A. Nel, T. Xia, L. Mädler, N. Li, Science **311**, 622 (2006)
[23] R. Di Corato, D. Palumberi, R. Marotta, M. Scotto, S. Carregal-Romero, P. Rivera Gil, W.J. Parak, T. Pellegrino, Small **8**, 2731 (2012)
[24] P. Dallas, J. Tucek, D. Jancik, M. Kolar, A. Panacek, R. Zboril, Adv. Funct. Mater. **20**, 2347 (2010)
[25] L. Wang, J. Luo, S. Shan, E. Crew, J. Yin, C.J. Zhong, B. Wallek, S.S. Wong, Anal. Chem. **83**, 8688 (2011)
[26] L. Zhang, Q. Luo, F. Zhang, D.M. Zhang, Y.S. Wang, Y.L. Sun, W.F. Dong, J.Q. Liu, Q.S. Huo, H.B. Sun, J. Mater. Chem. **22**, 23741 (2012)
[27] R. Massart, IEEE Trans. Magn. **17**, 1247 (1981)
[28] A. Ebrahiminezhad, Y. Ghasemi, S. Rasoul-Amini, J. Barar, S. Davaran, Bull. Korean Chem. Soc. **33**, 3957 (2012)
[29] Y.D. Yin, Z.Y. Li, Z.Y. Zhong, B. Gates, Y.N. Xia, S. Venkateswaran, J. Mater. Chem. **12**, 522 (2002)
[30] X.A. Li, J.J. Lenhart, H.W. Walker, Langmuir **26**, 16690 (2010)
[31] S.F. Chin, K.S. Iyer, C.L. Raston, Cryst. Growth Des. **9**, 2685 (2009)
[32] P. Lee, D. Meisel, J. Phys. Chem. **86**, 3391 (1982)
[33] T. Mosmann, J. Immunol. Methods **65**, 55 (1983)
[34] K. Eskandari, H. Ghourchian, J. Iran. Chem. Soc. **10**, 1 (2013)
[35] M. Mandal, S. Kundu, S.K. Ghosh, S. Panigrahi, T.K. Sau, S.M. Yusuf, T. Pal, J. Colloid Interface Sci. **286**, 187 (2005)
[36] D. Caruntu, G. Caruntu, Y. Chen, C.J. O'Connor, G. Goloverda, V.L. Kolesnichenko, Chem. Mater. **16**, 5527 (2004)
[37] C. Hui, C. Shen, J. Tian, L. Bao, H. Ding, C. Li, Y. Tian, X. Shi, H.J. Gao, Nanoscale **3**, 701 (2011)
[38] Q. Lu, K. Yao, D. Xi, Z. Liu, X. Luo, Q. Ning, J. Mater. Sci. Technol. **23**, 189 (2007)
[39] S. Shrivastava, T. Bera, A. Roy, G. Singh, P. Ramachandrarao, D. Dash, Nanotechnology **18**, 1 (2007)
[40] A.J. Kora, S.R. Beedu, A. Jayaraman, Org. Med. Chem. Lett. **2**, 1 (2012)
[41] N.T. Trang, T.T. Thuy, K. Higashimine, D.M. Mott, S. Maenosono, Plasmonics **8**, 1177 (2013)
[42] J. Sun, S. Zhou, P. Hou, Y. Yang, J. Weng, X. Li, M. Li, J. Biomed. Mater. Res. **80**, 333 (2007)
[43] R. Augustine, K. Rajarathinam, Int. J. Nano Dimens. **2**, 205 (2012)
[44] K. Can, M. Ozmen, M. Ersoz, Colloids Surf. B **71**, 154 (2009)
[45] G.M.G. Ennas, A. Musinu, J. Mater. Res. **14**, 1570 (1999)
[46] Z.S. Pillai, P.V. Kamat, J. Phys. Chem. B. **108**, 945 (2004)
[47] H.L. Liu, S.A. Dai, K.Y. Fu, S.H. Hsu, Int. J. Nanomed. **5**, 1017 (2010)
[48] C. Carlson, S.M. Hussain, A.M. Schrand, L.K. Braydich-Stolle, K.L. Hess, R.L. Jones, J.J. Schlager, J. Phys. Chem. B **112**, 13608 (2008)